ARTICLE   OPEN

Check for updates

A hybrid triboelectric nanogenerator for enhancing corrosion prevention of metal in marine environment

Menzhen Wu[1], Wenxi Guo[2✉], Shigang Dong[1], Andeng Liu[3], Yanhui Cao[3,4], Zijie Xu[5], Changjian Lin [3,6✉] and Jian Zhang[1]

A hybrid spherical triboelectric nanogenerator (S-TENG) with both solid-solid and solid-liquid contact modes is successfully constructed to collect wave energy for highly efficient cathodic protection of metals in marine. To maximize collection of wave energy, the S-TENG is designed to simultaneously capture friction energy from inside and outside the device with different working modes, achieving a short circuit current density of 186 mA m^{-3} and open circuit voltage of 88.9 V, respectively. It indicates that the potential drop of stainless steel (304SS) and organically coated carbon steel (Q235CS) coupled with the S-TENG are about 410 mV and 930 mV, respectively, which is suitable for their cathodic protection in marine environment. It is demonstrated that our S-TENG as a low-cost and environmentally friendly self-powered approach is promising to effectively converts wave energy for electrochemical cathodic protection in marine.

INTRODUCTION

Marine environment is known as the most corrosive natural medium in the world, which results in huge loss of economy and blocking marine progress as well[1,2]. With the development and utilization of marine resources costing an increasing proportion of the fiscal expenditure, various metals have been widely used in the marine environment, and the inevitable corrosion of infrastructure and industrial facilities is increased serious, which has become the most crucial factor affecting the safety, reliability and life of ships, offshore engineering and deep-sea equipment[3]. Therefore, the protection of metals in the ocean from corrosion is significantly meaningful in economic development[4]. So far, anti-corrosion coatings and electrochemical cathodic protection are two main methods to protect metals from corrosion, which are usually used in combination in commercial buildings and marine facilities[2,5,6]. Electrochemical cathodic protection is recognized as one of the most effective ways to protect the metals from corrosion in ocean[4,7]. Traditional electrochemical cathodic protection can be divided into impressed current cathodic protection (ICCP) and sacrificial anode cathodic protection (SACP). The former is that the metal is protected by cathodic current from an external power source, while the latter is protected by the cathodic current generated by anodic dissolution[8,9]. For the ICCP system, an uninterrupted external power supply is needed to provide sufficient output over a period of time, which will increase costs and cause environmental pollution. As for the SACP system, more active metals are lost and the area of protected metals is limited to the size of the sacrificed metals[4,10]. In addition, it is difficult to supply the power required for cathodic protection and sacrificial anodes in the open sea and islands. Therefore, it is a prospective and challenging task to develop a green, low-cost and efficient energy system to harvest wave energy from marine for achieving effective metal cathodic protection[5,11,12].

Ocean waves are one of the most abundant and continuous energy sources on the earth, but it belongs to irregular low-frequency energy, harvesting such energy is rather difficult due to the efficiency of traditional electromagnetic generators (EMG), which is directly proportional to the square of frequency, remains very low in wave energy collection[13]. Recently, a new type of mechanical energy collecting device called triboelectric nanogenerator (TENG), based on the working principle of coupling effect of triboelectrification and electrostatic induction[14], has attracted wide attention[15–22]. In contrast with EMG system, the TENG had demonstrated higher energy conversion efficiency in low-frequency irregular mechanical vibration, plus its advantages on lightweight of devices, simple preparation, extensive material selection and reliability, enabling it to capture wave energy and to be applied in the ocean[23–29]. Additionally, as a potential new type of application[30,31], the TENG has been introduced in the ICCP system as the external power source these years[3–5,32–36]. These TENGs can be summarized into two working modes: the one is based on solid–solid contact-separation mode which needs effective packaging technology to isolate water; the other is solid-liquid contact-separation mode which is based on the triboelectrification between the water and polymers. Previous works mainly focused on the TENG in single working mode[4,10], which is relatively simple and the application scenarios are limited.

Here, we designed a hybrid spherical triboelectric nanogenerator (S-TENG) with both solid–solid and solid-liquid contact modes, which can effectively collect low frequency wave energy for metal corrosion protection in marine environment. The S-TENG is composed of two different working modes, which can markedly increase the energy conversion efficiency and total output performance since both the inner and the outer surfaces of spherical are effectively utilized. In this special self-powered cathodic protection system, the S-TENG is expected to replace conventional power source for ICCP system to drive

[1]Fujian Research Center for Nuclear Engineering, College of Energy, Xiamen University, Xiamen, Fujian 361002, PR China. [2]Research Institution for Biomimetics and Soft Matter, College of Physical Science and Technology, Fujian Provincial Key Laboratory for Soft Functional Materials Research, Xiamen University, Xiamen 361005, PR China. [3]State Key Laboratory of Physical Chemistry of Solid Surfaces, Department of Chemistry, College of Chemistry and Chemical Engineering, Xiamen University, Xiamen, Fujian 361005, PR China. [4]State Key Laboratory for Marine Corrosion and Protection, Luoyang Ship Material Research Institute, Xiamen 361101, PR China. [5]CAS Center for Excellence in Nanoscience, Beijing Key Laboratory of Micro-nano Energy and Sensor, Beijing Institute of Nanoenergy and Nanosystems, Chinese Academy of Sciences, Beijing 101400, PR China. [6]Tan Kah Kee Innovation Laboratory, Xiamen, Fujian 361005, PR China. ✉email: wxguo@xmu.edu.cn; cjlin@xmu.edu.cn
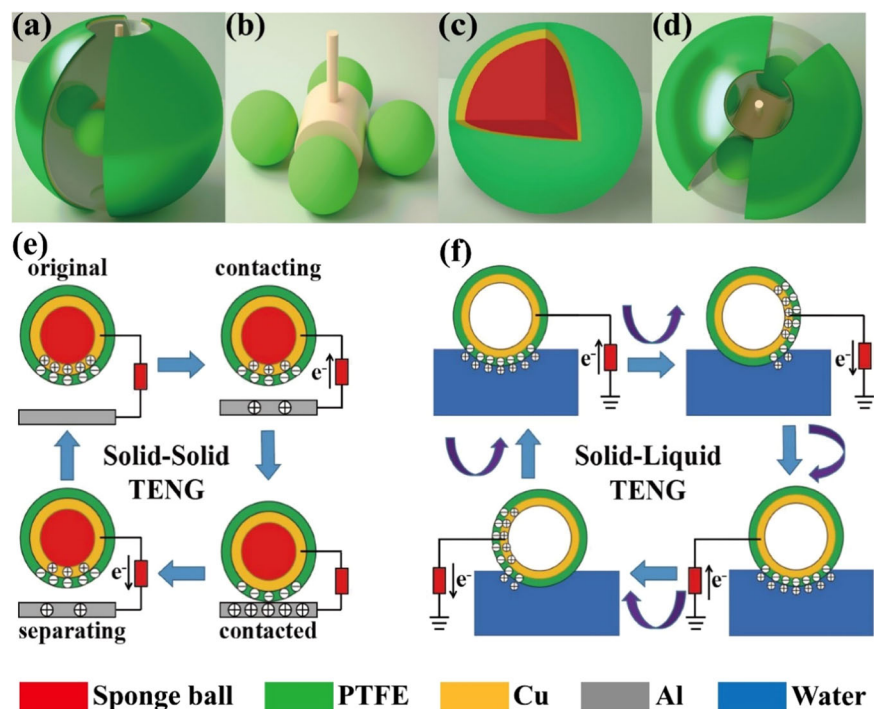
Fig. 1 Schematic illustration of the design and principle of S-TENG. a Schematic illustration of the S-TENG. **b** Schematic structure of S-TENG in the inner. **c** Detailed structure of sponge balls. **d** Overhead view of the S-TENG. Operation principle of the inner solid–solid TENG (**e**) under contact–separation mode. Operation principle of the outer solid-liquid TENG (**f**) under single electrode mode.

charges to the coupled metals, providing effectively cathodic protection for stainless steel (304SS) and carbon steel (Q235CS) in simulated marine.

RESULTS AND DISCUSSION

Construction of S-TENG

The spherical triboelectric nanogenerator (S-TENG) as schematically shown in Fig. 1a is mainly composed of two components: the inner solid-solid TENG and the outer solid–liquid TENG. For the solid–solid TENG, some sponge balls are placed inside the hollow plastic sphere and sway periodically with the movement of waves. The outer solid–liquid TENG is a single electrode mode TENG, which is driven by contact-separation of water and polytetrafluoroethylene (PTFE). The detailed fabrication process of the S-TENG device can be found in the Methods and the photos of the real devices is illustrated in Supplementary Fig. 1. It is worth mentioning that a pendulum is placed inside the sphere and swings periodically with the fluctuation of sea water, so that drives the sponge balls for periodical contact and separation movement with the inner surface of the spherical. This integrated design is able to effectively make full use of the outer and inner friction surface of the spherical, improve the space utilization of the spherical structure and obviously enhance the output performance of TENG.

The operation mechanism of the S-TENG is mainly based on the conjugation of triboelectrification and electrostatic induction. Figure 1e describes the operation principle of the inner solid–solid TENG. Accompanying the back and forth movement of the sponge ball, the Al foils on the inner surface of the plastic sphere is in contact–separation with the PTFE–Cu films on the surface of sponge ball. Due to the different abilities of attracting electrons between Al and PTFE, the Al foils are connected as the positive output end and all the Cu electrodes under PTFE films are connected together as the negative output end. At the beginning, there is no charge between the PTFE film and the Al

electrode. When the device was driven by water waves, the distance between the Al foil and the PTFE film starts to decrease and the potential difference between the two surfaces is established, driving electrons from the Al foil to the Cu electrode under the PTFE film and generate an instantaneous current. When the PTFE film is in full contact with the Al electrode, the charge is neutralized. As the S-TENG continued to oscillate with the sea waves, the Al foil is separated from the PTFE film and the potential difference is established again, the electron on the PTFE film were transferred to the Al foil until new balance is achieved. Correspondingly, a current with reverse direction would be generated.

The operation principle of the solid–liquid TENG under single electrode mode for harvesting water wave energy is depicted in Fig. 1f. Similarly, due to the different abilities of attracting electrons between PTFE and water, they become negatively charged and positively charged after contacting with each other. Electrical potential difference is produced when the PTFE film is rotating across the water air interface. Electrons driven by the electrical potential difference are forced to flow between the Cu electrode and ground, generating output current flow.

Surface treatment of PTFE film

For solid-liquid TENG, it is important to have good hydrophobicity on the friction material surface, because the residual water on the material surface would reduce the power generation capacity[37]. Constructing microstructures on the electrode surface can not only increase the friction area, but also improve the hydrophobicity. Here, the surface of PTFE films were treated with emery papers and their scanning electron microscope (SEM) images are displayed in Fig. 2a, b. It is clear that the surface roughness of PTFE film is increased after roughening with emery papers. The surface hydrophobicity of PTFE film was evaluated by water contact angle measurements, from Fig. 2c and d, it can be seen that the contact angle between the PTFE film and deionized water increases from 108° to 132° after be treated with emery papers, and not residual
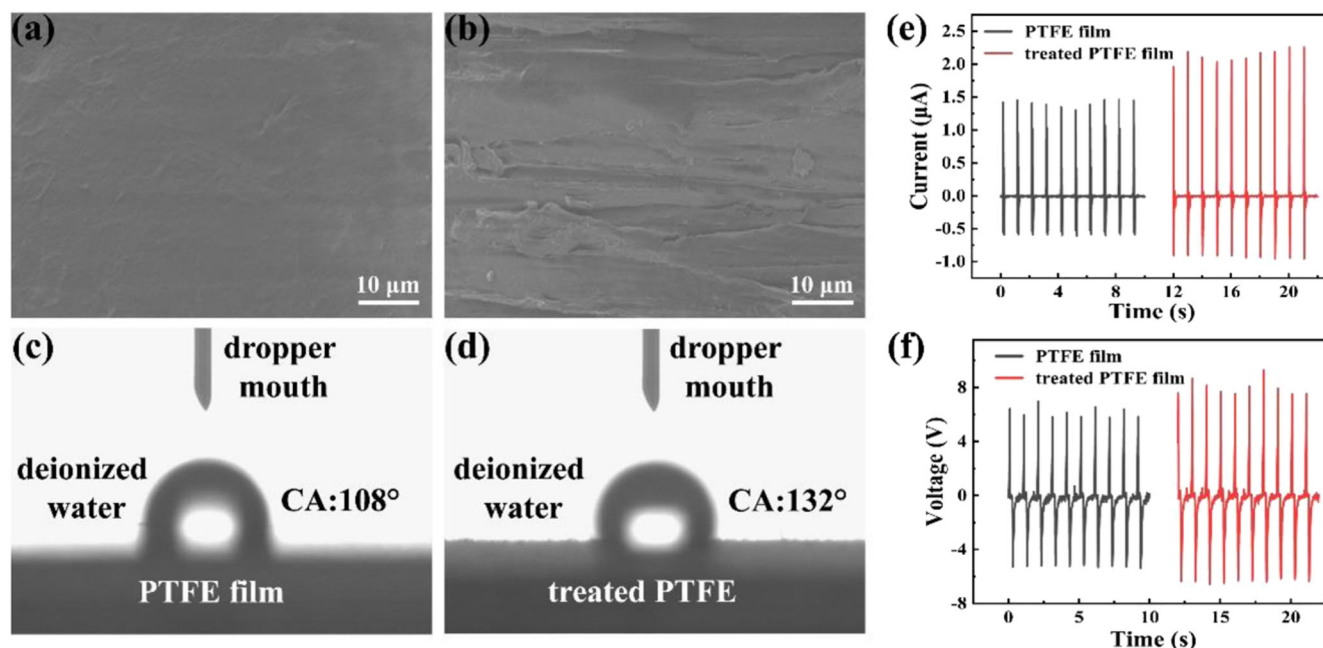
Fig. 2 The performance of PTFE film after surface treatment. SEM image of the PTFE film before (**a**) and after (**b**) being polished with emery papers. The hydrophobicity images of deionized water drop on a PTFE film before (**c**) and after (**d**) being polished with emery papers. Short-circuit current (**e**) and open-circuit voltage (**f**) between the two dielectric materials of PTFE film and Al foil.

water adsorbed on the surface. This result can be explained by the Wenzel's equation (Eq. 1)[38,39].

$$\cos \theta_1 = r \cos \theta_2 \qquad (1)$$

where θ_1 is Wenzel apparent contact angle, θ_2 corresponds to real contact angle on a smooth surface, and r represents ratio of the actual surface to the geometric surface, that is called surface roughness factor. According to the equation, it can be found that when θ_2 is less than 90°, the surface is hydrophilic, increase of the surface roughness will lead to a lower θ_1. On the contrary, when θ_2 is more than 90°, the surface is hydrophobic, the increase of the surface roughness will induce a higher θ_1. The result of PTFE film surface roughness and contact angle, as shown in Fig. 2, are consistent with this conclusion. In addition, the linear motor was used to simulate the motion of ocean waves, at the frequency of 1 Hz, the comparison of output performance for the TENG with roughened and smooth PTFE film is shown in Fig. 2e, f. Both short-circuit currents (I_{SC}) and open-circuit voltages (V_{OC}) of the PTFE film treated with emery papers are higher than that without treatment, indicating that the output performance of PTFE film increases after roughening.

Electrical characterizations of S-TENG

To follow the working behavior of S-TENG, the device was tested in a tank that simulates the motion of ocean waves. Figure 3 presents the output performance of the S-TENG with different numbers of sponge balls in the hollow plastic spherical. Both short-circuit currents (I_{SC}) and open-circuit voltages (V_{OC}) of solid-solid TENG as shown in Fig. 3c, d, respectively, increase as the number of sponge balls increase, i.e., the highest value of I_{SC} and V_{OC} increased from 95.8 μA to 174 μA and 9.6 V to 14.6 V, respectively, when the number of the sponge balls increased from 4 to 6. This phenomenon is due to the fact that increasing contact area between PTFE film on the sponge balls and Al electrodes would increase the amount of charge by separated contact. Constrained by the limited space, the optimal number of the sponge balls with a diameter of 40 mm in the S-TENG, which with a diameter of 16 cm, is approximately six. Figure 3e, f

shows the output performance of the solid-liquid TENG with I_{SC} and V_{OC} of approximately 150 μA and 60 V, respectively. The output performance of S-TENG as shown in Fig. 3g, h, when the number of the sponge balls increases from 4 to 6, the peak value of I_{SC} and V_{OC} also increase from 237 μA to 399 μA and 73.6 V to 88.9 V, respectively. As the current outputs of the S-TENG shows alternating current (AC) characteristic, it is required to be rectified. Figure 3i is a rectifier circuit diagram for TENG, and the current output of the S-TENG after rectified is about 220 μA as shown in Fig. 3j. What's more, from Fig. 3k, it is obvious that the S-TENG remains stable after continuous operation of 400,000 cycles and its output in enhanced after working for a long time. The result is due to charge accumulation effect on the surface of PTFE triboelectrode and also indicates that the S-TENG device possesses good stability in simulated marine. The harvested wave energy can be stored in the different capacitors as shown in Fig. 3l. The capacitors with capacities ranging from 1 μF to 47 μF are charged to 15 V, and the required time length is increased from 2 s to 7 min.

Cathodic protection system based on the S-TENG

Figure 4a show schematic arrangement of the wave-powered cathodic protection system based on the S-TENG. When the water wave drives the S-TENG to start working, the electrons generated by triboelectrification is transferred to the metals in sea water, resulting in cathodic polarization to a certain extent. In this wave-powered cathodic protection system, potential shift is a key parameter to value the performance of cathodic protection[5]. In short, more electrons transferred leads more negative shift of the potential of the metals and more effective cathodic protection. A three-electrode system is used to test the potential variation of the 304 stainless steel (304SS) coupled with and without TENG. From Fig. 4b, without TENG, the potential of the 304SS in 3.5 wt% NaCl solution is about −0.21 V (vs. SCE) and it dropped rapidly to −0.47 V (vs. SCE) and −0.52 V (vs. SCE) when the 304SS was connected to solid-solid TENG and solid-liquid TENG, respectively, then slowly restored to their original potential when TENGs disconnected. As expected, while the 304SS is connected with the S-TENG, the protection potential shifted to −0.62 V, presenting
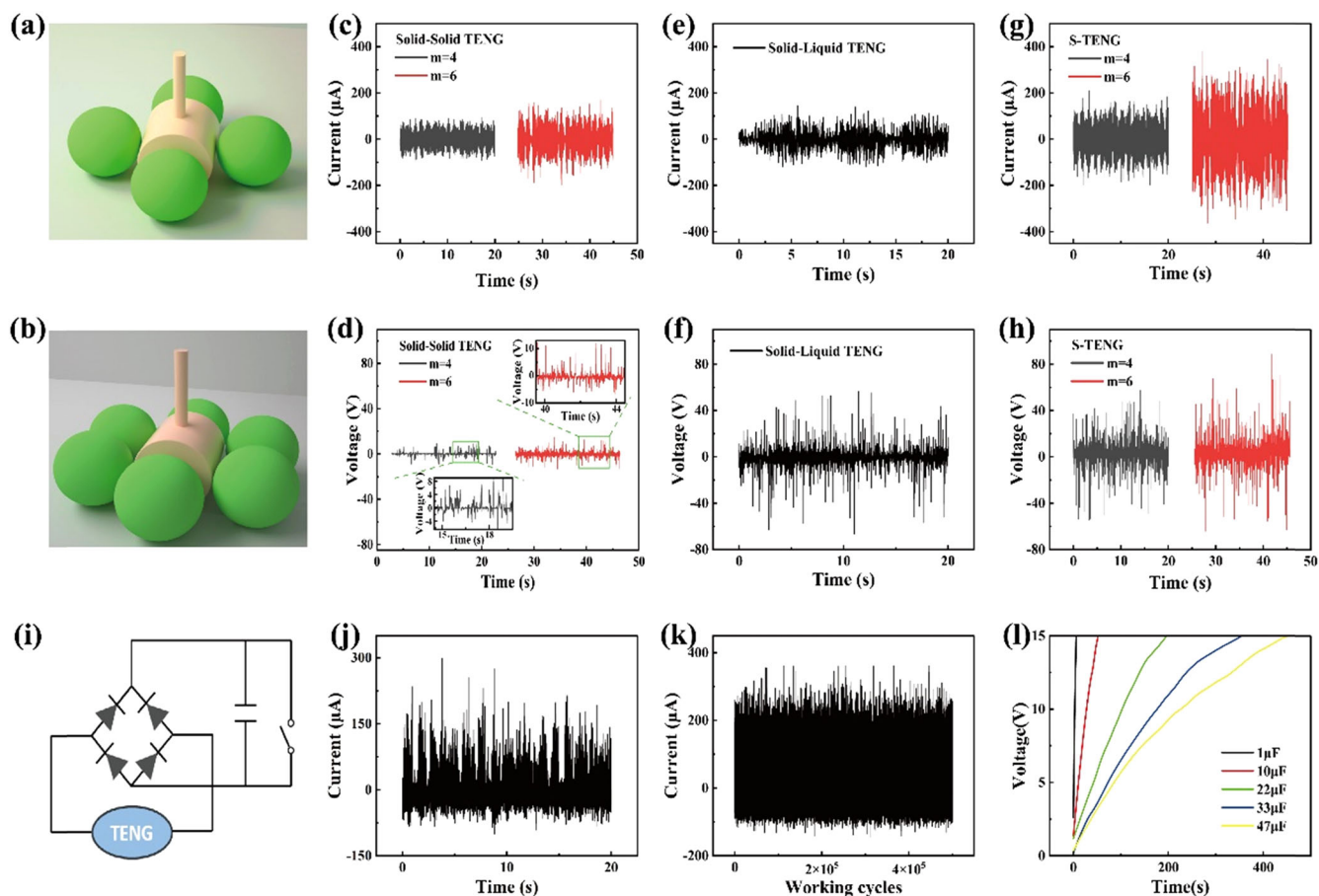
Fig. 3 The electrical characterizations of S-TENG. a and **b** Schematic diagram of sponge balls with different numbers. Short-circuit current (**c**) and open-circuit voltage (**d**) of the solid-solid TENG with different numbers of sponge balls. Short-circuit current (**e**) and open-circuit voltage (**f**) of the solid-liquid TENG. Short-circuit current (**g**) and open-circuit voltage (**h**) of the S-TENG with different numbers of sponge balls. **i** Schematic diagram of rectifier circuit of TENG. **j** The rectified current of the S-TENG. **k** Stability test of the S-TENG. **l** The charging curves of different capacitors charged by the S-TENG in the wave tank equipment.

more efficient cathodic protection than any single working-mode TENG. The periodic variation of the potential indicates that the high repeatability of the self-powered cathodic protection system driven by different mode of TENGs. Moreover, in Fig. 4c, after two hours of continuous protection with S-TENG in the wave tank, the protection potential of the 304SS maintains at −0.62 V and further indicates the stability of the cathodic protection system. The immersion tests of 304SS in 3.5 wt% NaCl solution as shown in Fig. 4d, e were carried out to further investigate the cathodic protection performance. At the beginning of immersion, the protection potential of 304SS shifted negatively by 0.34 V. It is obvious that the protection potential shift of 304SS increased from 0.34 V to 0.49 V as increasing the immersion time, and it remained stable after 7 days. The positive shift of protection potential can be attributed to the self-repair and growth of passive film on 304SS when immersed for the first 0–4 days, that is, with the increase of immersion time, the protection current required by 304SS gradually decreases. When the immersion time exceeds 4 days, the effect of cathodic protection reaches the peak and tends to be stable, that is, the protection current required also tends to be stable. Furthermore, the metal electrode with different area coupled with and without S-TENG was tested to study the relationship between protection potential changes and the area of protected metal. As shown in Fig. 4g, with the exposure area of 304SS increase from 0.79 cm² to 5.31 cm², the negative shift of protection potential decrease from 0.38 V to 0.11 V when connected with the S-TENG. From the fitting curve in Fig. 4h,

it can be clearly seen that the shift of protection potential of 304SS shows a good negative linear relationship with its area. The equation (Eq. 2) corresponding to the fitting curve is as follow:

$$y = 0.41 - 0.057x \qquad (2)$$

where y is the shift of protection potential of 304SS when connected with S-TENG, x is the exposure area of 304SS electrode. According to the reported of Sun et al.[40], the protection potential of 304SS ranged from −0.47 V to −0.8 V, that is, the protection provided by S-TENG is effective only when the shift of potential of 304SS reaches at least 260 mV. Therefore, our device (the volume is about 2144.66 cm³) can provide effectively cathodic protection for 1.77 cm² of 304SS in simulated marine. When the area of 304SS greater than 1.77 cm², it is required to responsively enlarge S-TENG scale.

For Q235 carbon steel (Q235CS), the combination of cathodic protection and organic coating is commonly used to protect it from corrosion in marine environment[41]. The barrier effect of the coating can largely reduce the current density required for cathodic protection, and cathodic protection can maintain effective protection even if the coating locally damaged[42]. The cathodic protection potential of carbon steel is usually required from −0.77 V to −1.1V[43]. From Fig. 5i, it can be seen that when the thickness of waterborne acrylic coating is r = 25 μm, the protection potential of Q235CS connected with S-TENG is within the effective protection range. As shown in Fig. 4j, the S-TENG is able to provide effectively cathodic protection for 7.07 cm² of Q235CS in simulated marine, and the shift of protection potential of
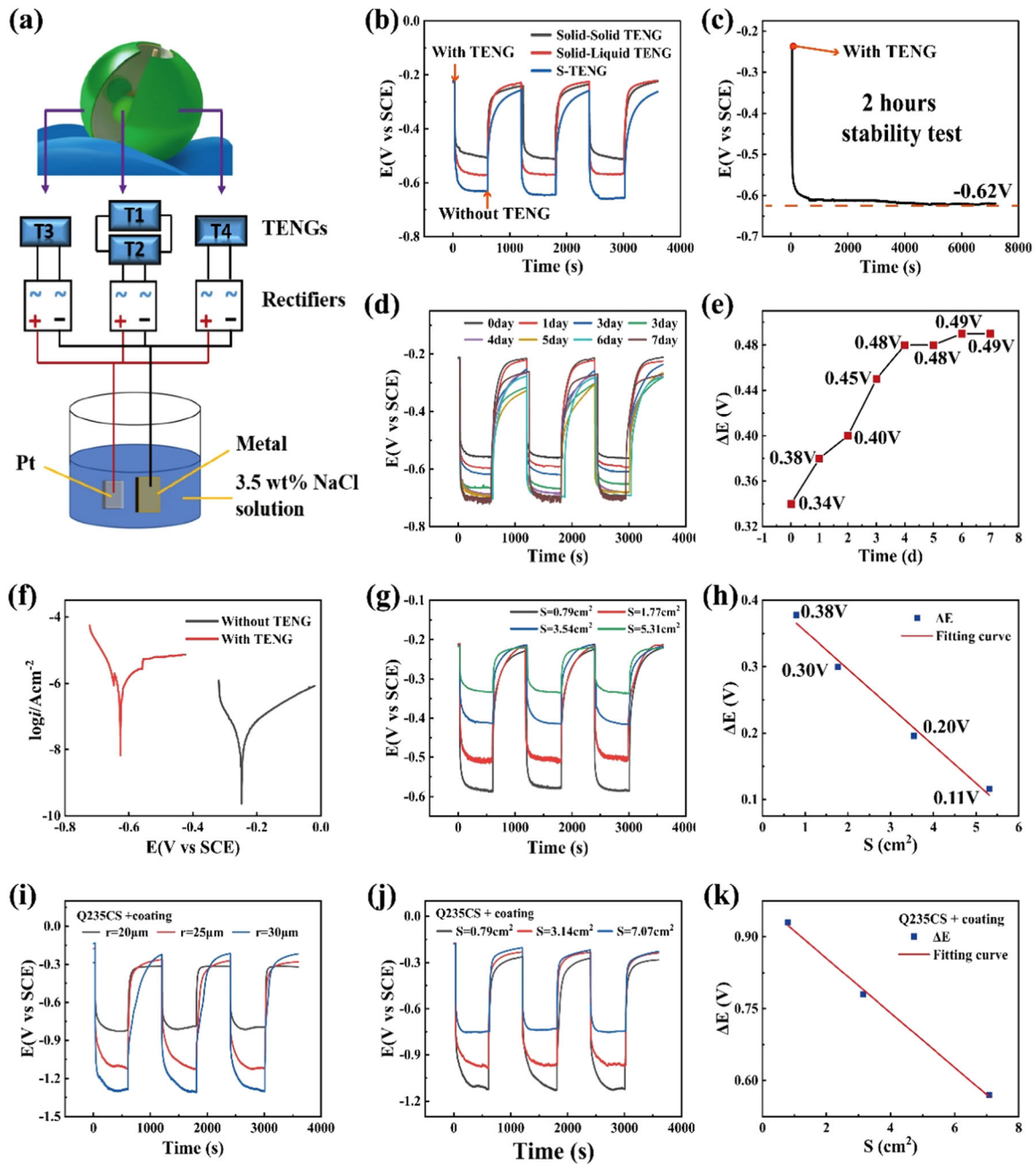
Fig. 4 **The cathodic protection performance of S-TENG. a** Schematic arrangement of the S-TENG cathodic protection of metal in 3.5 wt% NaCl solution. **b** Potential changes of a 304SS electrode coupled with and without solid-solid TENG, solid-liquid TENG and S-TENG respectively. **c** Stability test of the S-TENG. **d** Potential changes of a 304SS electrode coupled with and without S-TENG at different immersion time. **e** Potential drop value of 304SS at different immersion time. **f** Tafel curves of 304SS with and without S-TENG. **g** Potential changes of 304SS electrodes with different areas coupled with and without S-TENG. **h** Potential drop value of 304SS with different areas and its fitting curve. **i** Potential change of a Q235CS electrode coupled with and without S-TENG at different the coating thickness. **j** Potential changes of Q235CS electrodes with different areas coupled with and without S-TENG. **k** Potential drop value of Q235 with different areas and its fitting curve.

Q235CS also shows a good negative linear relationship with its exposure area. The equation (Eq. 3) corresponding to the fitting curve is as follow:

$$y = 0.97 - 0.057x \tag{3}$$

where y is the shift of protection potential of Q235CS when connected with S-TENG, x is the area of Q235CS electrode.

Tafel polarization curves are usually adopted to study the corrosion rate by measuring the corrosion potential and corrosion current density. Figure 4f shows the Tafel plots of the 304SS

connected with and without the S-TENG and its corresponding electrochemical parameters including corrosion potential, corrosion current density, anodic Tafel slope (b_a) and cathodic Tafel slope (b_c) listed in Table 1. In the cathodic protection system, the larger negative shift of corrosion potential indicates that more electrons flow to 304SS and thus, the stronger cathodic protection effect can be achieved. The corrosion potential of the 304SS is about -0.23 V and -0.64 V (vs. SCE) without and with S-TENG. The results indicate that the corrosion resistance of 304SS could be effectively improved by cathodic protection system driven by
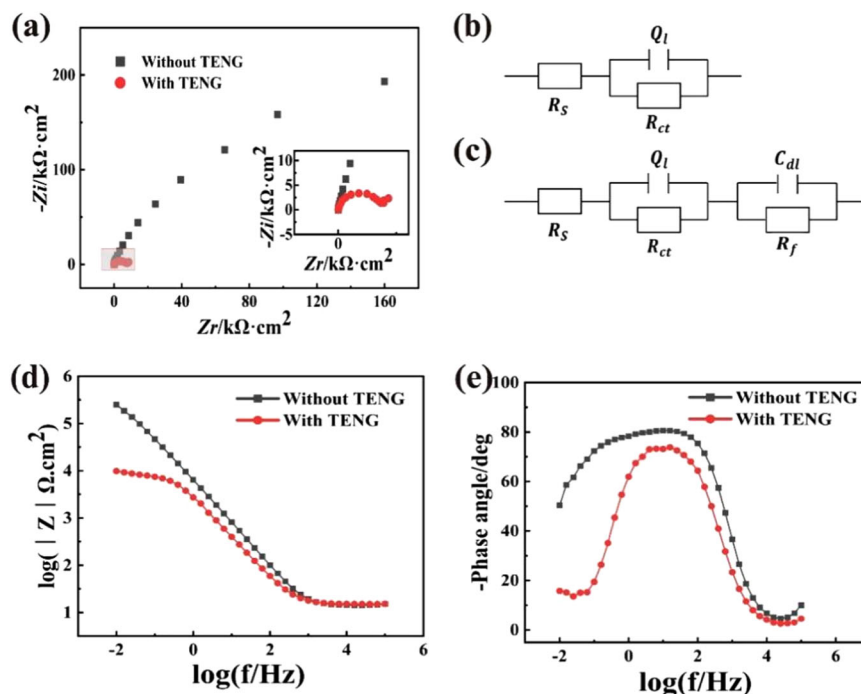
Fig. 5 The EIS of 304SS. a Nyquist curves of 304SS with and without cathodic protection powered by the S-TENG. **b** The equivalent circuit of 304SS connected without the S-TENG and (**c**) the equivalent circuit of 304SS connected with the S-TENG. **d** Impedance-frequency Bode plots and (**e**) Phase-frequency Bode plots of 304SS with and without cathodic protection powered by the S-TENG.

Table 1. Electrochemical parameters obtained from Tafel curves of 304SS connected with and without the S-TENG.

Sample	E_{corr}/V (vs.SCE)	j_{corr}/μA cm^{-2}	b_a/mV dec^{-1}	b_c/mV dec^{-1}
Without TENG	−0.23	0.0073	34.66	−25.98
With TENG	−0.63	0.293	28.23	−26.84

S-TENG. What's more, as shown in Table 1, compared with the 304SS without S-TENG, the corrosion current density of 304SS with S-TENG increased by ~40 times. It can be concluded that the electrochemical reaction is accelerated by injecting electrons produced by S-TENG into the surface of 304SS. The above results are in good agreement with the potential as shown in Fig. 4b. In conclusion, the Tafel plot shows that the cathodic protection system driven by S-TENG can improve corrosion resistant performance by injecting a large amount of electrons into the surface of 304SS.

The arc of Nyquist plot corresponding to the 304SS with S-TENG as shown in Fig. 5a is much smaller than that without S-TENG. Besides, according to Fig. 5d, it is obvious that the low frequency impedance modulus of the 304SS with S-TENG is nearly two orders of magnitudes lower than that without S-TENG. In Fig. 5e, the maximum phase angle of 304SS with S-TENG becomes smaller and narrower than that of without S-TENG, which can be attributed to the effect of injection of external electrons. Here, the equivalent circuit of the S-TENG protection system and the value of each component are obtained through curve fitting, and the electrochemical reaction mechanism and kinetic process are described qualitatively and quantitatively. The CPE (constant phase element) is normally used to analyze the impedance spectrum of the actual electrode process under non-ideal conditions. There are two important parameters of CPE in equivalent circuit: admittance Y and power index number n, the formula is $Y = Y_0(j\omega)^n$. When n is equal to 0, CPE is turn into pure resistance, and when n is equal to 1,

CPE is turn into pure capacitance. In general, the value of n is between 0 and 1. Figure 5b exhibits the equivalent circuit of 304SS without the S-TENG described as $R_s(Q_lR_{ct})$. More specifically, Q corresponds to CPE, R_s represents electrolyte resistance and R_{ct} represents charge transfer resistance. Figure 5c shows the equivalent circuit of 304SS with the S-TENG described as $R_s(Q_lR_{ct})(C_{dl}R_f)$. Specifically, R_f corresponds to the 304 stainless steel/solution interface layer resistance and C_{dl} corresponds to the double-layer capacitance. The detail electrochemical parameters of the equivalent circuit are displayed in Table 2, in which R_{ct} value of the 304SS with S-TENG is much lower than that of the 304SS without S-TENG. Due to the R_{ct} is equal to the charge transfer resistance, a smaller R_{ct} represents faster electron transfer to the metals, resulting from the reciprocating oscillation of the S-TENG.

The immersion tests of Q235CS was carried out in simulated seawater to investigate the practical effect of corrosion protection. Figure 6 shows the digital photographs of the surface morphology of the Q235CS with and without S-TENG after immersing in 3.5 wt % NaCl solution at different times. It is obvious by naked eye that much more rust appeared on the Q235CS without S-TENG than that with S-TENG at different immersion time. Generally speaking, once corrosion happened on Q235CS surface the corrosion rate increases rapidly and more and more rust expands on the surface. When the immersion time was extended to 6 h in the 3.5 wt% NaCl solution, the Q235CS without S-TENG is corroded in a large area, while only some corrosion spots appeared on the Q235CS with S-TENG. The results prove that the self-powered system based on the S-TENG can effectively reduce the corrosion rate, that is, the cathodic protection system powered by the S-TENG is an effective anti-corrosion method.

METHODS

Materials and chemicals

The polytetrafluoroethylene (PTFE) films (thickness: 100 μm) were acquired from Shenzhen Huasheng Plastic Material Co., Ltd. Sodium chloride (GR ≥ 99.5%) was obtained from Xilong Science Co., Ltd. The double-sided

Table 2. Electrochemical impedance parameters for 304SS with and without impressed current cathodic protection powered by the S-TENG in 3.5 wt % NaCl solution.

Samples	$R_s(\Omega cm^2)$	Q		$R_{ct}(k\Omega cm^2)$	$C_{dl}(\mu F)$	$R_f(k\Omega cm^2)$
		$Y_0(10^{-5}\Omega cm^{-2}S^n)$	n			
Without TENG	14.08	3.142	0.8947	441.2	–	–
With TENG	15.03	6.528	0.8777	5.754	5.249	8.425
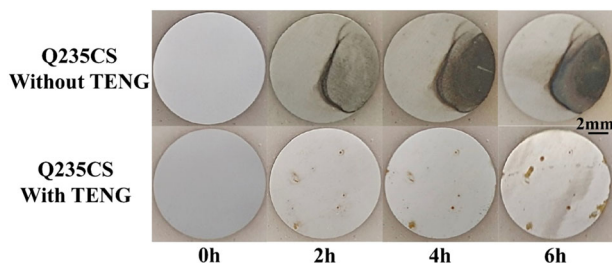
Fig. 6 The digital photographs of Q235 carbon steels. The surface morphology of Q235 carbon steels immersed in 3.5 wt% NaCl solution for 2 h, 4 h and 6 h, separately, connected without and with the S-TENG.

conductive copper foil tape (thickness: 65 μm) was acquired from Shenzhen Mileqi Adhesive Tape Co., Ltd. Sponge balls (diameter: 40 mm) was obtained from Shenzhen Luyi Golf Products Company. Wooden pendulum was fabricated from a handmade bamboo shop. Hollow plastic hemispherical shell (diameter: 16 cm) was acquired from Jinhua festival supplies store. Al foil (thickness: 15 μm) was acquired from Shanghai Klinglay Plastics Co., Ltd. The waterborne acrylic resin coatings was obtained from Left and right hands paint flagship store.

Fabrication of the spherical TENG

The spherical triboelectric nanogenerator (S-TENG) is mainly composed of solid-solid TENG and solid-liquid TENG. The solid-solid TENG consist of two hollow plastic hemispherical shells with Al electrodes on their inner surfaces (Supplementary Fig. 1), which are attached and encapsulated together to form the complete hollow plastic ball. Some sponge balls with conductive copper foil tape covered by PTFE film are stuck around the wooden pendulum, which is located in the center of hollow plastic sphere. The joint between the two hollow plastic hemispheres shells is sealed with PTFE sealing tape and transparent adhesive tape to prevent water leakage into the hollow plastic sphere. The PTFE film as the friction layer, the copper foil tape as electrodes, Al foil as another friction layer and electrode. Meanwhile, the contact of outer surface of two hollow plastic hemispherical shells, which with Cu electrodes covered by PTFE film, and dynamic water are designed to form a solid-liquid TENG. The PTFE film and dynamic water as the two friction layers, the one electrode is Cu and another is connected ground.

Characterization

The surface morphologies of PTFE films were observed by scanning electron microscope (SEM, Hitachi SU-70). A contact angle (CA) meter (DSA-100) was applied to measure contact angle at room temperature. The output voltage and current of the device was tested by a digital meter (Keithley 6514) and the data was collected by LabVIEW software. The nanogenerator would generate a series of voltage and current signals under the action of periodic external forces.

Measurements of the self-powered cathodic protection system

The 304 stainless steel and Q235 carbon steel were polished by emery papers from grade 400 to 2000 and Al_2O_3 powder with diameters of 1.0 μm and 0.3 μm, and then used as the protected metals. For the organic coated Q235 carbon steel, one side of the sample was sandblasted and polished as the working surface, cleaned and dried with ethanol after acetone degreasing, and then the waterborne acrylic coating with different

thickness was applied on the sample and cured for 24 h. The relevant electrochemical experiments including open circuit potential (OCP), electrochemical impedance spectroscopy (EIS) and Tafel plots were measured by the electrochemical workstation (Autolab) in a three-electrode system. A platinum sheet works as the counter electrode, the reference electrode is a SCE (saturated calomel electrode), metals work as the working electrode. The amplitude of the EIS was set as 10 mV and the frequency range was set as 10^{-2}Hz-10^5Hz. The EIS data were analysed using ZView 3.1. Tafel plots were tested at a sweep rate of 0.167 mV s^{-1} and in the sweep range of −120 mV to 120 mV vs. OCP (SCE). The above experiments were carried out in the 3.5 wt% NaCl solution.

DATA AVAILABILITY

Data that support the findings presented in this manuscript can be provided upon reasonable request by contacting the corresponding author.

REFERENCES

1. Wang, H. et al. A self-healing polyurethane-based composite coating with high strength and anti-corrosion properties for metal protection. *Compos. B. Eng.* **225**, 109273 (2021).
2. Kumari, S., Saini, A. & Dhayal, V. Metal oxide based epoxy coatings for corrosion protection of steel. *Mater. Today.: Proc.* **43**, 3105–3109 (2021).
3. Wang, Z., Cheng, L., Zheng, Y. B., Qin, Y. & Wang, Z. L. Enhancing the performance of triboelectric nanogenerator through prior-charge injection and its application on self-powered anticorrosion. *Nano Energy* **10**, 37–43 (2014).
4. Guo, W. X. Electrochemical cathodic protection powered by triboelectric nano-generator. *Adv. Funct. Mater.* **24**, 6691–6699 (2014).
5. Sun, W. X. et al. Liquid-solid triboelectric nanogenerators array and its applications for wave energy harvesting and self-powered cathodic protection. *Energy* **217**, 119388 (2021).
6. Varela, F., Tan, M. Y. J. & Forsyth, M. Understanding the effectiveness of cathodic protection under disbonded coatings. *Electrochim. Acta* **186**, 377–390 (2015).
7. Cheung, M. M. S. & Cao, C. Application of cathodic protection for controlling macrocell corrosion in chloride contaminated RC structures. *Constr. Build. Mater.* **45**, 199–207 (2013).
8. Xu, J. & Yao, W. Current distribution in reinforced concrete cathodic protection system with conductive mortar overlay anode. *Constr. Build. Mater.* **23**, 2220–2226 (2009).
9. Yehia, S. & Host, J. Conductive concrete for cathodic protection of bridge decks. *ACI Mater. J.* **107**, 577–585 (2010).
10. Li, X. Y. et al. A self-powered system based on triboelectric nanogenerators and supercapacitors for metal corrosion prevention. *J. Mater. Chem. A* **3**, 22663–22668 (2015).
11. Li, X. G. et al. Materials science: share corrosion data. *Nature* **527**, 441–442 (2015).
12. Guan, Z. C., Zhao, J. Z., Guo, W. X., Du, R. G. & Lin, C. J. Research progresses in "green" electrochemical cathodic protection. *J. Xiamen Univ. (Nat. Sci.)* **59**, 767–777 (2020).
13. Zi, Y. L. et al. Harvesting low-frequency (<5 Hz) irregular mechanical energy: a possible killer application of triboelectric nanogenerator. *ACS Nano* **10**, 4797–4805 (2016).
14. Rodrigues, C. et al. Emerging triboelectric nanogenerators for ocean wave energy harvesting: state of the art and future perspectives. *Energy Environ. Sci.* **13**, 2657–2683 (2020).
15. Feng, Y. G. et al. Paper-based triboelectric nanogenerators and their application in self-powered anticorrosion and antifouling. *J. Mater. Chem. A* **4**, 18022–18030 (2016).
16. Li, X. Y., Lau, T. H., Guan, D. & Zi, Y. L. A universal method for quantitative analysis of triboelectric nanogenerators. *J. Mater. Chem. A* **7**, 19485–19494 (2019).

17. Zhu, G. et al. A shape-adaptive thin-film-based approach for 50% high-efficiency energy generation through micro-grating sliding electrification. *Adv. Mater.* **26**, 3788–3796 (2014).

18. Zhu, G. et al. Harvesting water wave energy by Asymmetric Screening of electrostatic charges on a nanostructured hydrophobic thin-film surface. *ACS Nano* **8**, 6031–6037 (2014).

19. Qin, Y., Wang, X. D. & Wang, Z. L. Microfibre–nanowire hybrid structure for energy scavenging. *Nature* **451**, 809–813 (2008).

20. Tian, J. W., Chen, X. Y. & Wang, Z. L. Environmental energy harvesting based on triboelectric nanogenerators. *Nanotechnology* **31**, 32092711 (2020).

21. Chen, J. H. et al. Design optimization of soft-contact freestanding rotary triboelectric nanogenerator for high-output performance. *Adv. Energy Mater.* **11**, 2102106 (2021).

22. Chen, J. H. et al. Self-powered antifouling UVC pipeline sterilizer driven by the discharge stimuli based on the modified freestanding rotary triboelectric nanogenerator. *Nano Energy* **95**, 106969 (2022).

23. Cui, S. W., Zheng, Y. B., Liang, J. & Wang, D. A. Conducting polymer PPy nanowire-based triboelectric nanogenerator and its application for self-powered electrochemical cathodic protection. *Chem. Sci.* **7**, 6477–6483 (2016).

24. Lei, R. et al. Butterfly-inspired triboelectric nanogenerators with spring-assisted linkage structure for water wave energy harvesting. *Adv. Mater. Technol.* **4**, 1800514 (2019).

25. Yao, Y. Y. et al. Charging system optimization of triboelectric nanogenerator for water wave energy harvesting and storage. *ACS Appl. Mater. Inter.* **8**, 21398–21406 (2016).

26. Xu, L. et al. Coupled triboelectric nanogenerator networks for efficient water wave energy harvesting. *ACS Nano* **12**, 1849–1858 (2018).

27. Wang, X. et al. Fully packaged blue energy harvester by hybridizing a rolling triboelectric nanogenerator and an electromagnetic generator. *ACS Nano* **10**, 11369–11376 (2016).

28. Xi, Y. et al. High efficient harvesting of underwater ultrasonic wave energy by triboelectric nanogenerator. *Nano Energy* **38**, 101–108 (2017).

29. Wang, H. Y. et al. A fully-packaged ship-shaped hybrid nanogenerator for blue energy harvesting toward seawater self-desalination and self-powered positioning. *Nano Energy* **57**, 616–624 (2019).

30. Luo, J. J. & Wang, Z. L. Recent progress of triboelectric nanogenerators: From fundamental theory to practical applications. *EcoMat* **2**, e12059 (2020).

31. Wang, Z. L. Triboelectric nanogenerators as new energy technology for self-powered systems and as active mechanical and chemical sensors. *ACS Nano* **7**, 9533–9557 (2013).

32. Zhang, Y. Y. et al. Organosulfonate counteranions—a trapped coordination polymer as a high-output triboelectric nanogenerator material for self-powered anticorrosion. *Chem. Eur. J.* **26**, 584–591 (2020).

33. Zhu, H. R. et al. Self-powered metal surface anti-corrosion protection using energy harvested from rain drops and wind. *Nano Energy* **14**, 193–200 (2015).

34. Zhang, H. L. et al. Simultaneously harvesting thermal and mechanical energies based on flexible hybrid nanogenerator for self-powered cathodic protection. *ACS Appl. Mater. Inter.* **7**, 28142–28147 (2015).

35. Cui, S. W., Zheng, Y. B., Liang, J. & Wang, D. A. Triboelectrification based on double-layered polyaniline nanofibers for self-powered cathodic protection driven by wind. *Nano Res.* **11**, 1873–1882 (2018).

36. Zhao, X. J., Zhu, G., Fan, Y. J., Li, H. Y. & Wang, Z. L. Triboelectric charging at the nanostructured solid/liquid interface for area-scalable wave energy conversion and its use in corrosion protection. *ACS Nano* **9**, 7671–7677 (2015).

37. Liu, Y. P., Zheng, Y. B., Li, T. H., Wang, D. A. & Zhou, F. Water-solid triboelectrification with self-repairable surfaces for water-flow energy harvesting. *Nano Energy* **61**, 454–461 (2019).

38. Gao, N. & Yan, Y. Y. Modeling superhydrophobic contact angles and wetting transition. *J. Bionic Eng.* **6**, 335–340 (2009).

39. Cao, Y. H. et al. Enhanced corrosion resistance of superhydrophobic layered double hydroxide films with long-term stability on Al Substrate. *ACS Appl. Mater. Inter.* **10**, 15150–15162 (2018).

40. Sun, T. X., Huang, G. S., Lv, P., Xu, L. K. & Ma, L. Evolution of calcareous deposits and passive film on 304 stainless steel with cathodic polarization in sea water. *Coatings* **8**, 8050194 (2018).

41. Ranade, S., Forsyth, M. & Tan, M. Y. J. In situ measurement of pipeline coating integrity and corrosion resistance losses under simulated mechanical strains and cathodic protection. *Prog. Org. Coat.* **101**, 111–121 (2016).

42. Rendón Belmonte, M. et al. Characterization of steel surface under cathodic protection in seawater. *Anti-Corros. Method M.* **60**, 160–167 (2013).

43. Zhao, Z. Y., Lv, W. Y., Liu, C., Ma, Y. Q. & Kong, A. M. Application study of combining both cathodic protection and organic coating in corrosion protection of offshore oil facilities in deep sea. *Total Corros. Control* **26**, 20–22 (2012).

ACKNOWLEDGEMENTS

AUTHOR CONTRIBUTIONS

M.W. carried out the experiment and A.L. assisted with a part of measurements. M.W. was supervised by C.L. and she wrote the manuscript with support from W.G., S.D., Y.C. and C.L. And Z.X. provided graphing technique. All authors discussed the results.

COMPETING INTERESTS

The authors declare no competing interests.

ADDITIONAL INFORMATION

Supplementary information The online version contains supplementary material available at https://doi.org/10.1038/s41529-022-00272-y.

Correspondence and requests for materials should be addressed to Wenxi Guo or Changjian Lin.

Reprints and permission information is available at http://www.nature.com/reprints

Publisher's note Springer Nature remains neutral with regard to jurisdictional claims in published maps and institutional affiliations.